X-ray absorption spectra of graphene and graphene oxide by full-potential multiple scattering calculations with self-consistent charge density

Junqing Xu,[1] Peter Krüger,[2] Calogero R. Natoli,[3] Kuniko Hayakawa,[3] Ziyu Wu,[1,4,*] and Keisuke Hatada[3,5,6,†]

[1]*National Synchrotron Radiation Laboratory, University of Science and Technology of China, Hefei, Anhui 230026, China*

[2]*Graduate School of Advanced Integration Science, Chiba University, Chiba 263-8522, Japan*

[3]*INFN Laboratori Nazionali di Frascati, Via E. Fermi 40, C.P. 13, I-00044 Frascati, Italy*

[4]*Beijing Synchrotron Radiation Facility, Institute of High Energy Physics, CAS, Beijing 100049, China*

[5]*Département Matériaux Nanosciences, Institut de Physique de Rennes, UMR UR1-CNRS 6251, Université de Rennes 1, 35042 Rennes Cedex, France*

[6]*Physics Division, School of Science and Technology, Università di Camerino, via Madonna delle Carceri 9, I-62032 Camerino (MC), Italy*

(Received 10 June 2015; published 9 September 2015)

The x-ray absorption near-edge structure of graphene, graphene oxide, and diamond is studied by the recently developed real-space full potential multiple scattering (FPMS) theory with space-filling cells. It is shown how accurate potentials for FPMS can be generated from self-consistent charge densities obtained with other schemes, especially the projector augmented wave method. Compared to standard multiple scattering calculations in the muffin-tin approximation, FPMS gives much better agreement with experiment. The effects of various structural modifications on the graphene spectra are well reproduced. (1) Stacking of graphene layers increases the peak intensity in the higher energy region. (2) The spectrum of the C atom located at the edge of a graphene sheet shows a prominent pre-edge structure. (3) Adsorption of oxygen gives rise to the so-called *interlayer*-state peak. Moreover, O K-edge spectra of graphene oxide are calculated for three types of bonding, C-OH, C-O-C, and C-O, and the proportions of these bondings at 800 °C are deduced by fitting them to the experimental spectrum.

DOI: 10.1103/PhysRevB.92.125408 PACS number(s): 78.70.Dm, 61.48.Gh, 71.15.Ap

I. INTRODUCTION

Due to its exceptional electronic structure, mechanical strength, and high electrical conductivity [1], graphene is expected to become a key material for future nanotechnologies. Graphene oxide (GO) is also widely used for reasons of synthesis and chemical stability. X-ray absorption spectroscopy (XAS) and electron energy loss spectroscopy (EELS) are invaluable tools to study the electronic and atomic structure of defects and adsorbates of graphene layers [2–4]. However, because of the existence of various competing structures and the lack of accurate theoretical calculations, the origin of the observed spectral features is generally not well understood yet.

XAS and EELS of graphene have been computed previously using density functional theory (DFT) implemented for ground-state electronic structure calculations [5,6]. These methods usually rely on periodic boundary conditions, so that the asymptotic behavior of the wave function may be not reproduced well for low-dimensional systems in particular directions, and use fixed basis sets whose convergence for high-energy states may be problematic. Also, the energy-dependent quasiparticle self-energy is replaced with the DFT ground exchange-correlation potential (V_{xc}). Concerning these problems, the multiple scattering (MS) method has clear advantages, because the single-particle Schrodinger equation is solved with the exact numerical basis functions for each energy. As a consequence, basis function convergence is not an issue and inclusion of energy-dependent self-energies is straightforward. Moreover, the MS method is easily implemented in reciprocal space, real space, and mixtures thereof, which makes it a method of choice for low-dimensional and nanostructured systems.

Conventional MS theory relies on the muffin-tin (MT) approximation, where the potential is assumed to be spherically symmetric in each atomic (MT) sphere and constant outside the spheres, that is, in the so-called interstitial region. The MT approximation is quite poor for graphene-like systems for the following reasons: (i) The charge density of the C-C σ and π bonding is highly anisotropic. (ii) For light elements such as carbon, atomic potential scattering is rather weak and thus scattering of the interstitial potential is comparatively strong. Hence full potential (FP) corrections are important. (iii) The available energy range for x-ray absorption fine structure of light elements is limited to a few tens of eletron volts. This near-edge region shows rich spectral features due to the strong scattering effects and the peaks are sharp because of the long core-hole lifetimes. Therefore, the FP and self-consistent field (SCF) are necessary to increase the precision of the calculations.

Here we report x-ray absorption near-edge structure (XANES) calculations of ideal and defective graphene, GO, and diamond, using the real-space full potential (FP) multiple scattering (FPMS) theory with arbitrarily truncated space-filling cells [7,8]. We also present a method to generate all-electron potentials for FPMS from accurate charge densities provided by other electronic structure codes, in particular, projector augmented wave method (PAW) methods [9]. This allows us to access the importance of FP corrections and self-consistency in MS calculations of C K-edge XANES. The results are in good agreement with experiment and shed light on the origin of some controversial features of graphene XANES.

*Deceased 23 March 2015.

†keisuke.hatada@univ-rennes1.fr

II. THEORY

A. FPMS method

There have been many attempts to extend the MS theory to the FP level [10–15]. Here we give a brief summary of the FPMS method developed previously by some of us [7]. The real-space FPMS theory with space-filling cells used here is valid for both continuum and bound states and contains only one truncation parameter, $l$max, the maximum angular momentum of the spherical wave basis. Space is partitioned by nonoverlapping space-filling cells or Voronoi polyhedra. When a Voronoi polyhedron does not contain any atom or is in the interstitial region but still contains charge density, it is called an empty cell (EC). The local Schrodinger equation is solved without the limit of the geometrical shape of the potential since the potential is not expanded in spherical harmonics. The absorption cross section is given by

$$\sigma(\omega) = -8\pi\alpha\hbar\omega \sum_{m_c} \mathrm{Im} \int \left\langle \phi^c_{L_c}(\vec{r}) \middle| \hat{\varepsilon}\cdot\vec{r} \middle| G(\vec{r},\vec{r'};E) \middle| \times \hat{\varepsilon}\cdot\vec{r'} \middle| \phi^c_{L_c}(\vec{r}) \right\rangle d\vec{r}\, d\vec{r'},$$

where $\phi^c_{L_c}$ is the initial core state, with $L_c \equiv (l_c,m_c)$ representing the orbital angular momentum and magnetic quantum number, ω is the frequency of incident light, α is the fine-structure constant, $\hat{\varepsilon}$ is the electric-field direction of incident light, and E is the energy of the final state. Green's function can be written as

$$G(\vec{r}_i,\vec{r}'_j;E) = \langle \underline{\Phi}(\vec{r}_i) | ([I - GT]^{-1}G)^{ij} | \underline{\Phi}(\vec{r}'_j) \rangle - \delta_{ij} \langle \underline{\Phi}(\vec{r}_<) | \Psi(\vec{r}_>) \rangle,$$

where $\vec{r}_i$ is the coordinate with respect to the center of scattering site i. T and G, on the right-hand side of the equation, are the matrix of transition operators of scattering sites and KKR real-space structure factors, respectively. $\underline{\Phi}_L \equiv \sum_{L'} (\tilde{E})^{-1}_{LL'} \Phi_{L'}$, where Φ is the solution of the local Schrodinger equation which behaves as the first kind of spherical Bessel function at the origin and the $\tilde{E}$ matrix can be computed using values on the surface of the cell. Ψ is the solution of the local Schrodinger equation irregular at the origin, which matches smoothly the spherical Hankel function at the cell boundary. $r_<$ ($r_>$) is the smaller (larger) of r and r'.

B. FPMS potentials from PAW charge densities

Plane-wave codes using the PAW method are popular because of their high accuracy and computational efficiency for total energy DFT calculations. In the PAW method, the all-electron Kohn-Sham potential is replaced with a pseudopotential inside the augmentation spheres around the nuclei. This pseudopotential coincides with the all-electron potential only in the space outside the augmentation sphere. However, for XANES calculations the all-electron potential is required in all space, especially near the nuclei, where the core orbital has a high amplitude. We now present a method for reconstructing the all-electron potential in augmentation spheres from the all-electron charge density, which is commonly provided in PAW methods, such as the Vienna Ab initio Simulation Package (VASP) [16] that we have used here. As the calculation of a local or semilocal exchange correlation potential from the charge density is straightforward, we only explain how to obtain the all-electron Hartree potential.

The mathematical problem is to find the regular solution of the Poisson equation inside an (augmentation) sphere S of radius r_c, with the Dirichlet boundary condition on the sphere; i.e., we want to solve

$$\nabla^2 V(\vec{r}) = -4\pi\rho(\vec{r})$$

for $r < r_c$, given the charge density ρ for all points inside S and the potential V on the surface ($r = r_c$). We introduce the function

$$W(\vec{r}) \equiv \int_S \frac{\rho(\vec{r'})}{|\vec{r} - \vec{r'}|}\, d\vec{r'},$$

which satisfies the Poisson equation but, in general, not the boundary condition. $W(\vec{r})$ can easily be calculated in a spherical harmonic basis,

$$W(r,\hat{r}) = \sum_L \omega_L(r) Y_L(\hat{r}),$$

$$\omega_L(r) = \int_0^{r_c} \frac{r^l_<}{r^{l+1}_>}\, \rho_L(r') 4\pi r'^2 dr',$$

$$\rho_L(r) = \int Y^*_L(\hat{r}) \rho(r,\hat{r})\, d\hat{r},$$

where $\hat{r} = \vec{r}/r$. The angular integrals can be performed very accurately on a Lebedev mesh [17]. The general solution of the Poisson equation is the sum of a particular solution, such as W, and the general solution of the corresponding homogeneous (i.e., Laplace) equation. The latter solution is $\sum_L C_L r^l Y_L(\hat{r})$ for arbitrary coefficients C_L. By choosing $C_L = [\upsilon_L(r_c) - \omega_L(r_c)]/r^l_c$, where

$$\upsilon_L(r) = \int Y^*_L(\hat{r}) V(r,\hat{r})\, d\hat{r},$$

the boundary conditions are satisfied, and so the final solution is given by

$$V(r,\hat{r}) = \sum_L \left(\omega_L(r) + [\upsilon_L(r_c) - \omega_L(r_c)] \frac{r^l}{r^l_c} \right) Y_L(\hat{r}).$$

This method has been implemented in the program VASP2MS, which reads the charge density ρ and the Hartree (pseudo-)potential [for $V(r_c,\hat{r})$] provided by the VASP code and calculates the all-electron Hartree potential in all space for use in the FPMS code. In practice, the following VASP files are used: `AECCAR0`, `-1`, and `-2`, which contain the core (-0), non-SCF valence (-1), and SCF valence (-2) charge density, respectively; and `LOCPOT`, which contains the Hartree pseudopotential inside the atomic spheres and true potential in the rest of the unit cell. The data in these files are stored on a regular three-dimensional grid of the unit cell. Further, `RADCHGC` and `RADCHGV` contain the core and valence charge density, expanded in spherical harmonics and stored on radial grids around each nucleus. In VASP2MS, the VASP Hartree potential (in `LOCPOT`) is interpolated onto the radial meshes used in FPMS, in the region outside the augmentation spheres. The all-electron charge density ρ is interpolated onto the FPMS mesh everywhere in the cluster. Then the method described above is applied to find the all-electron Hartree potential inside

TABLE I. Cartesian coordinates and radius of polyhedra of atoms and ECs in the unit cell of graphene and diamond. All data are in units of Å.

System and type	x	y	z	r
1. Graphene				
Carbon	1.424	0	0	0.95
Carbon	2.848	0	0	0.95
EC	0	0	±0.7	1.05
EC	1.068	±0.6166101	1.2	0.9
EC	1.068	±0.6166101	−1.2	0.9
EC	2.136	0	±1.2	0.9
2. Diamond				
Carbon	±0.445875	±0.445875	±0.445875	0.89175
EC	±1.337625	±1.337625	±1.337625	0.89175

the augmentation spheres. Finally, the exchange-correlation part of the potential is calculated from ρ and added to the Hartree potential.

C. Computational details

The C K-edge XANES spectra are calculated with the real-space MS method using the following forms of the potential.

(1) Non-SCF-FP: an FP calculation without self-consistency. The potential is calculated directly in the FPMS code and corresponds to the superposition of atomic charge densities.

(2) SCF-FP: a self-consistent FP calculation, where the potential has been reconstructed from the charge density obtained by the VASP code with the PAW [9] method.

(3) SCF-MT: the same as SCF-FP except that the MT approximation is applied.

The graphene layer is taken as the xy plane and the x axis along a carbon-carbon bond. The absorption cross section for light polarized along $a = x, y, z$ is denoted σ_a, $\sigma = (\sigma_z + \sigma_x + \sigma_y)/3$ is the unpolarized spectrum, and we define $\sigma_{x-y} = (\sigma_x + \sigma_y)/2$ as the in-plane ($z = 0$) cross section. For systems with $C3v$ point symmetry or higher, such as core-excited graphene, which has $D3h$ point symmetry, we have $\sigma_x = \sigma_y$. For an angle α between the electric field and the xy plane, the absorption cross section is $\sigma_\alpha = \sigma_z \sin^2\alpha + \sigma_x \cos^2\alpha$.

Table I lists the positions and spherical radii of atoms and ECs in the unit cells of graphene and diamond. Figure 1 is a schematic of the space partitioning used for graphene. The number of ECs is sufficient, as we have checked by adding two more EC layers, which did not change the XANES results. For the optical potential we take the Hedin-Lundqvist form [18], whose energy-dependent imaginary part accounts for damping effects through plasmon loss, with an additional constant imaginary potential accounting for the finite core-hole lifetime and leading to Lorentzian broadening. The lifetime broadening is 0.1 eV for C K-edge [19,20] and 0.15 eV for O K-edge [20,21] XANES, but in the case of graphene, the value 0.2 eV was also reported [22,23]. In order to better see the spectral fine structure at high energy, the imaginary part of the Hedin-Lundqvist potential has been omitted in a few cases (Figs. 5, 8, and 16). Moreover, the spectra are Gaussian

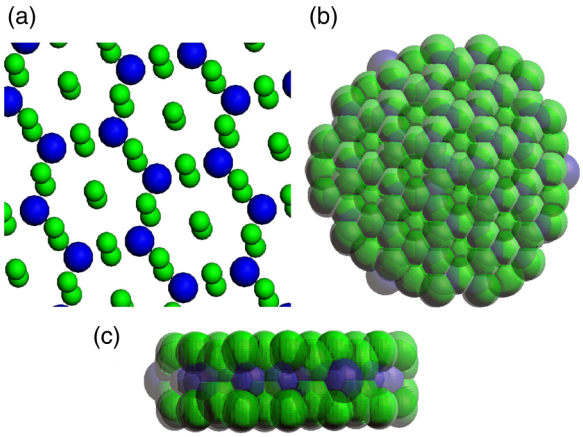

FIG. 1. (Color online) (a) Positions of carbon atoms (blue spheres) and empty cells (ECs; green spheres) for graphene. (b, c) Schematics of the graphene cluster with space-filling cells viewed along the z and y axis, respectively. The blue cell represents a carbon atom, and the green cell is an EC.

broadened by 0.4 eV (graphene) and 0.3 eV (diamond) in order to account for experimental effects such as instrumental errors, structural uncertainties, and vibration. From the convergence test, we take $l\max = 3$.

In Fig. 2 the effect of self-consistency on the ground-state charge density of graphene is shown for the $z = 0$ plane. Differences between SCF and non-SCF calculations are clearly visible, but the charge redistribution appears to be rather small.

Core-hole effects are treated using the so-called final-state rule; that is, in the final state the orbitals are relaxed around the full core hole. In non-SCF-FP, this relaxation is calculated self-consistently, but only at the atomic level. In SCF-FP, orbital relaxation effects beyond the absorbing atom are also taken into account through a VASP supercell (SC) calculation which yields the self-consistent final-state-rule charge density and electrostatic potential for the bulk material. In this case, the core electron is put into the lowest unoccupied molecular orbital and the frozen-core approximation is applied; i.e., only valence electrons are relaxed. In order to make the interaction between periodic images of the core-hole negligible, a large SC must be used. The converged size of the SC is found to be 4×4×1 for graphene and few-layer graphene (FLG) and 4×4×4 for diamond. However, for safety, larger SCs are used in this work, as listed in Table II.

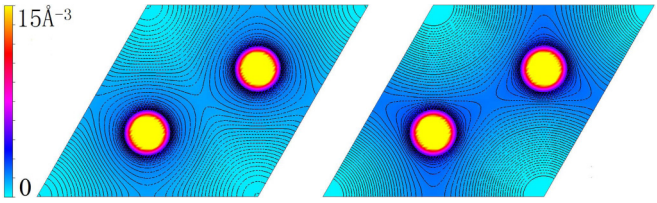

FIG. 2. (Color online) Charge density in the xy plane ($z = 0$) of the graphene unit cell from the non-SCF FPMS calculation (left) and the SCF (VASP) calculation (right). The unit of charge density is Å^{-3}. Contour lines are plotted for values $F_i = 5^{(-1+0.1i)}$ Å^{-3}, where $i = 0, 1, \ldots, 20$, from the corner to the region around carbon atoms.

TABLE II. Parameters used in VASP calculations.

	Graphene		Diamond	
Parameter	Core hole	No core hole	Core hole	No core hole
k points	3×3×1	15×15×1	1	11×11×11
E_{cut} (eV)	680	1100	680	1100
Supercell	5×5×1	1	5×5×5	1

Figure 3 shows the distribution of the differential all-electron valence charge densities in the xy plane, which are the differences between the density of a 5×5×1 SC of graphene with a core hole and that of ground-state graphene. It is shown that charge density redistribution is negligible for points farther than 2.5 Å from the core hole.

In the DFT VASP calculation, the gradient-corrected exchange-correlation functional PW91 [24] has been used but the local density approximation gives virtually identical results, as we have checked. The K-point sampling in the Brillouin zone and plane-wave cutoff energy (E_{cut}) are listed in Table II. For the SC dimension perpendicular to the layer, we took 15 Å, such that the interaction between periodic images of the graphene layer is negligible. When the VASP potentials are imported to the real-space cluster calculation, the final-state potential is used only for atoms not farther away from the absorbing site than some distance R, of the order of half the SC dimension. For atoms beyond R, the ground-state VASP potential is used. In this way the periodic repetition of core holes, which is an artifact of k-space methods (such as VASP) is avoided and convergence of the final results as a function of VASP SC size is very efficient.

III. XANES OF GRAPHENE

From Refs. [25] and [26], we have summarized the representative peaks of graphene and FLG in Table III. The calculated values correspond to the SCF-FP calculation with a cluster size of 30 Å. The theoretical energy scale has been rigidly shifted so as to align peak A with experiment (285.5 eV). Peaks A, B, and B2 were identified as the π^* resonance, σ^* resonance, and *excitonic*-state [27,28] peaks, respectively.

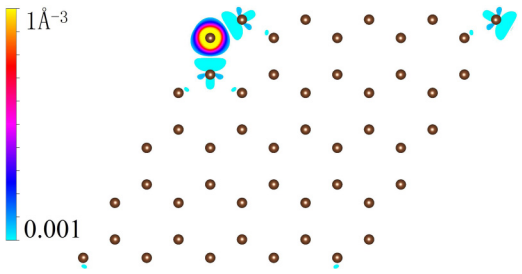

FIG. 3. (Color online) Valence charge density difference in the graphene xy plane, induced by a core hole in the top-left C atom of the 5×5×1 supercell. The unit of charge density is Å^{-3}. White corresponds to the value 0 and carbon atoms are represented by (brown) circles.

TABLE III. Peak positions of calculated (calc) XANES of graphene of 30 Å size in the SCF-FP case and experimental (exp) XANES of graphene and FLG. Peak H only exists in the experiment on FLG. (—) Not clear or not reproduced in calculations.

σ_z			σ_x		
Energy (eV)			Energy (eV)		
Calc	Exp	Symbol	Calc	Exp	Symbol
283.7	283.7	A2	–	291.7	B2
285.5	285.5	A	292.5	292.6	B
–	288.2	K	297.1	297.8	D
294.5	294.0	C	301.5	301.8	E
307.7	308.0	G	307.0	306.8	F
–	315.5	H	327.0	327.5	I

In Fig. 4 the experimental spectra [25,26] for two light polarizations are shown along with the present calculations done in different potential approximations. It is obvious that the FP calculations (non-SCF-FP or SCF-FP) agree much better with experiment than the MT calculation (SCF-MT). The differences between non-SCF-FP and SCF-FP spectra are small, indicating that self-consistency affects XANES much less than FP corrections. The peak positions of non-SCF-FP and SCF-FP spectra differ by about 1 eV and SCF-FP shows better agreement with experiment. Indeed, for out-of-plane polarization [$\alpha = 74°$; Fig. 4(a)] the SCF-FP calculation agrees very well with the data. However, a peak near 307.5 eV, labeled "F + G," appears in the SCF-FP result, but it is absent or faint in experiments [see Fig. 4(a)].

For in-plane polarization [$\alpha = 0°$; Fig. 4(b)] there is some systematic disagreement between experiment and all calculations, namely, overestimation of the peak B intensity and absence of peaks A and B2. The presence of peak A in the experimental data in Fig. 4(b) is very surprising, since peak A was identified in the σ_z spectrum [Fig. 4(a)] as the π^* resonance, which should exactly vanish for in-plane ($\alpha = 0°$) polarization (as it does in the calculations). This observation strongly suggests that some out-of-plane signal (σ_z) is mixed into the experimental spectra in Fig. 4(b). The reason may be a misalignment in the experiment or, more likely, the fact that the graphene layer is not perfectly flat [29], such that locally the electric field cannot be parallel to the graphene plane everywhere.

The leading low-energy peaks of the calculated spectra [peak A in Fig. 4(a) and peak B in Fig. 4(b)] are too intense, which indicates that charge relaxation around the core hole is overestimated. This might be due to the residual self-interaction in DFT [30]. Further, the excitonic state—peak B2 separated from peak B by about 1.0 eV—in the experiment is not reproduced in the calculations even if the Gaussian broadening is reduced to 0.2 eV. The theoretical problems with the leading peaks (B, B2) are likely related to the frozen-core approximation and to dynamical screening effects, i.e., the energy dependence of the complex self-energy [31,32]. The nonlocality of the particle-hole exchange interaction [33] is a further issue. It should be noted that the poor description of the leading peaks is a common problem for K-edge XANES

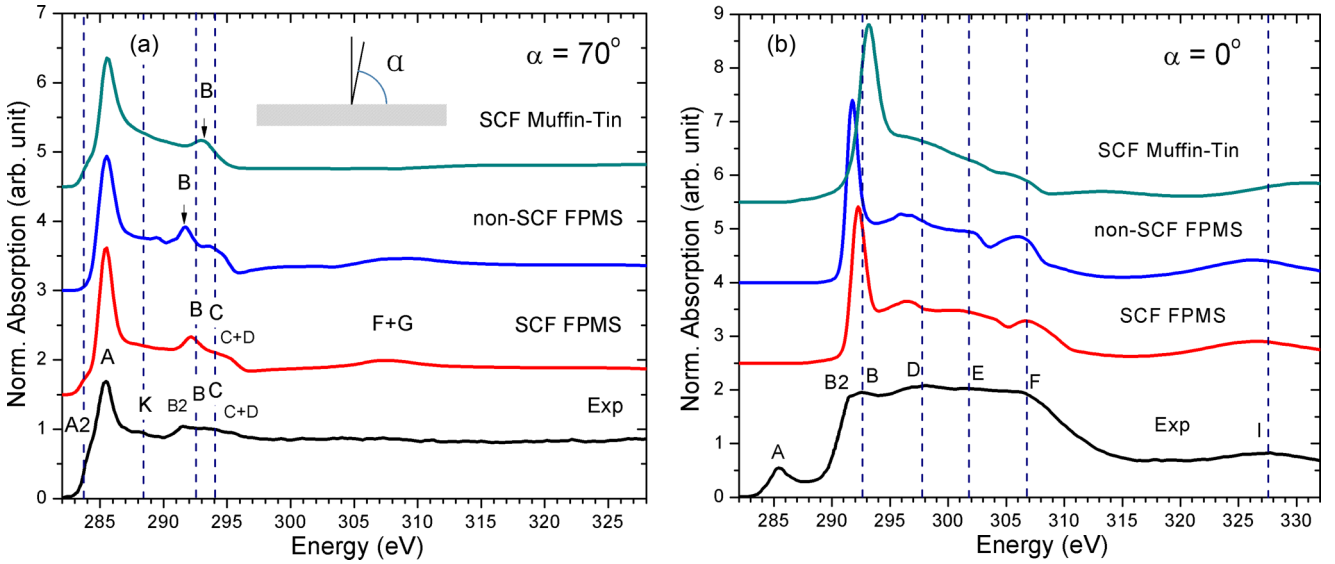

FIG. 4. (Color online) Comparison between calculated polarized C K-edge XANES of graphene with a cluster of radius 30 Å and experiments [25,26]. α is the angle between the electric field and the xy plane. (a) Since $\alpha = 74^\circ$, $\sigma \approx 0.924\sigma_z + 0.076\sigma_x$ (see Sec. II C). (b) The reason peak A arises despite the fact that $\alpha = 0^\circ$ is discussed in the text (Sec. III). Dashed vertical lines show the peak positions of experiments. SCF-FP, non-SCF-FP, and SCF-MT are defined in Sec. II C. (Non-)SCF represents using a (non-)self-consistent potential; FP and MT represent the full potential and muffin-tin versions of multiple scattering theory, respectively.

of light elements and has so far not been cured by any *ab initio* method we are aware of, including the Bethe-Salpeter equation approach [34].

Furthermore, in the experiment in Fig. 4(a), two weak peaks—a pre-edge one, A2, and peak K—were observed near 284 and 288 eV, respectively. In Ref. [25], peak A2 was attributed to a state about 0.8 eV below π^*, which was mentioned in a rather old density-of-states calculation for graphene [35]. However, in more recent density-of-states calculations [36–38], there does not exist any unoccupied state lower than the π^* state. We therefore believe that there is no such state in perfect graphene and that the observation of peak A2 in Ref. [25] was due to a structural imperfection. In Sec. III C we show that edge atoms can produce a feature similar to peak A2.

The origin of peak K has been contentious, and alternative descriptions ascribe it to residual functionalization [39,40], especially the bonding between carbon and oxygen, or a free-electron-like *interlayer* state [25,41]. In our SCF-FP result of XANES of the graphene cluster of radius 30 Å, for out-of-plane polarization [$\alpha = 74^\circ$; Fig. 4(a)], there is no distinct peak near 288 eV. Therefore, peak K probably will not arise in XANES of ideal graphene. Possible origins are discussed at the end of this section and in Sec. IV A.

A. Cluster size dependence

In the following, the theoretical spectra correspond to the SCF-FP method, unless stated otherwise. Figure 5 shows the cluster size dependence of the calculated spectra. Good convergence is achieved for a cluster radius of about 20 Å, except for some very fine features. Convergence is faster on the high-energy side of the spectrum, as is usually observed in real-space calculations for states above Fermi level.

We have found that the pre-edge peak, A2, and the oscillatory features between peak A and peak B can appear for small clusters, but as the cluster size increases, they become weaker. For a cluster radius of 30 Å, the features between peak A and peak B are gone. Therefore, finite size and vacancies in the graphene sheet may contribute to peaks A2 and K. However, we can expect these peaks to be negligible for graphene of a high structural quality, that is, perfectly flat sheets of several micrometers or larger with a low defect concentration.

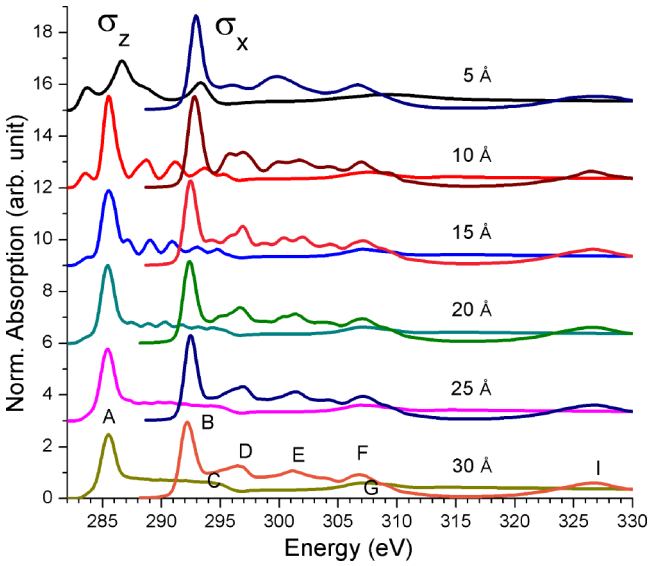

FIG. 5. (Color online) Calculated XANES in the SCF-FP case with different-sized radii of clusters whose center is the absorbing atom. $\sigma_{z(x)}$ is a polarized absorption cross section with an electric field along the z (x) axis.

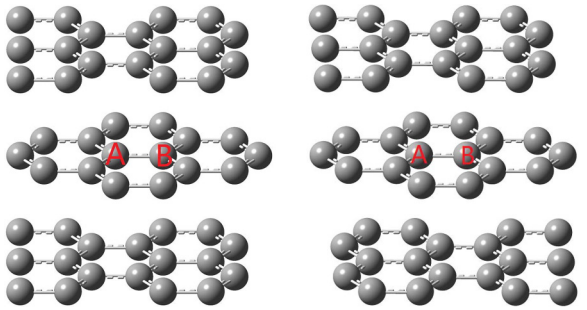

FIG. 6. (Color online) Schematic of Bernal (left) and rhombohedral (right) stacking of graphene layers.

B. Layer effects

In this section, XANES calculations of two-layer graphene (2LG), three-layer graphene (3LG), and graphite are reported. The cluster radius is 15 Å and the distance between layers is 3.4 Å. We consider Bernal stacking whose order is 1212 . . . [1] as shown in the left panel in Fig. 6. Each layer has two types of carbon atoms, A and B, giving a total of two types in both 2LG and graphite and four types in 3LG. The spectra of the different types are summed for comparison with experiment. The cluster potential is constructed using the strategy outlined above. Explicitly, for sites not farther than 6 Å from the absorber and in the same layer, the core-excited (SC) graphene VASP potential is used. For all other sites, the graphite VASP ground-state potential is used.

In order to check that this way of constructing the cluster potential is reliable, we have compared it with another strategy, where VASP potentials of both core-excited (SC) 3LG and ground-state 3LG are used. We found that both strategies give very similar results (not shown), which indicates that the charge density of a graphene layer is not much affected by the presence of other layers. Consistently, the spectral differences (not shown) between the inequivalent sites A and B is also small.

Apart from Bernal stacking, other stackings have been reported for multilayer graphene, most importantly rhombohedral stacking, whose order is 123123 . . . [1] (see right panel in Fig. 6). We have calculated the C K-edge XANES of 3LG in rhombohedral stacking but found only tiny differences from Bernal stacking. The differences appear to be too small for an experimental determination of the stacking sequence from the XANES results.

XANES of 3LG is shown in Fig. 7. The calculated peak intensities are systematically larger than in the data, but the positions of the peaks and their *relative* intensities are very well reproduced. In the calculated spectrum, a weak feature can be seen at 289 eV, close to the peak K energy. We note that the peak in the calculation is due to the finite cluster radius (15 Å) in the *xy* plane. In Fig. 8, graphene, 2LG, 3LG, and graphite are compared. When the number of layers goes up, peaks G, H, and J [42] increase quite strongly and peak C slightly, whereas peak A2 decreases somewhat. These tendencies agree well with experiment [25,26]. Moreover, the oscillatory features near 288.5 eV remain unchanged, which indicates that the effects of stacking of graphene layers on peak K is weak.

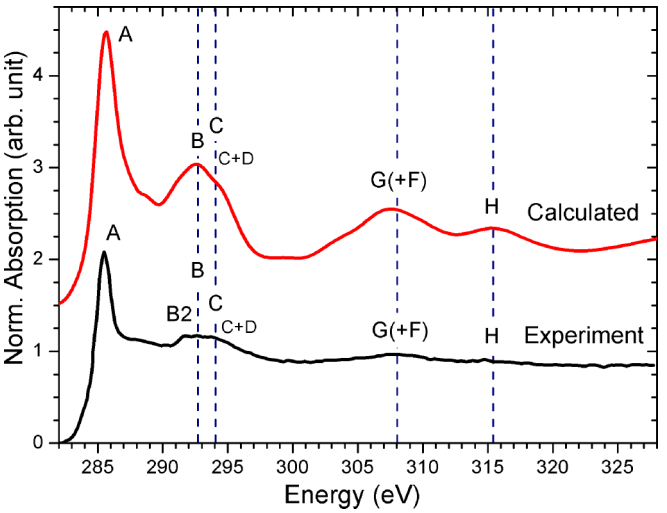

FIG. 7. (Color online) Comparisons between calculated polarized C K-edge XANES of 3LG with a cluster whose size is 15 Å and the experiment [25]. The angle between the electric field and the *xy* plane is also 74°. To achieve better agreement with the experiment, we used 0.7-eV Gaussian broadening.

C. Edge effects

One-dimensional structures such as graphene ribbons are interesting for potential applications. The reduced dimensionality and the presence of edge atoms can strongly modify the electronic and transport properties of graphene. The local electronic structure at the edge of a graphene has been measured by x-ray absorption microscopy [43] and EELS [44,45]. Here we study XANES of a zigzag-type edge terminated by hydrogen and focus on several particular kinds of carbon atoms, which are colored pink and labeled with numbers as shown in Fig. 9. Spectra are calculated using a cluster of the semi-infinite graphene zigzag edge of radius 25 Å around the absorber. Atomic positions at the edge are relaxed in a VASP calculation with a 1×22 SC containing 1 hydrogen and 22 carbon atoms along the axis perpendicular to the edge. The final-state potential is generated as follows.

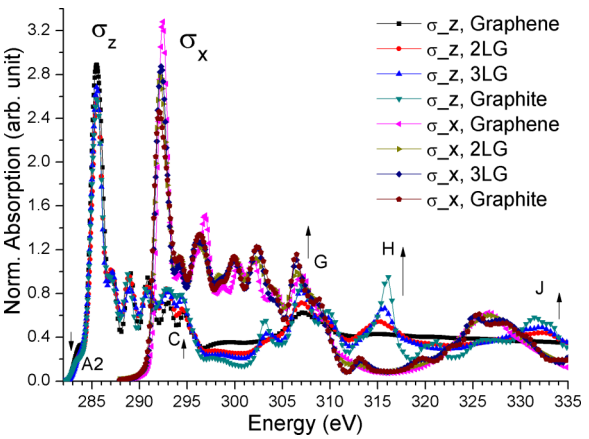

FIG. 8. (Color online) Calculated XANES of graphene, 2LG, 3LG, and graphite. $\sigma\_z(x)$ represents $\sigma_{z(x)}$. Arrows represent the variation trend of the peak intensity as the layer number increases.

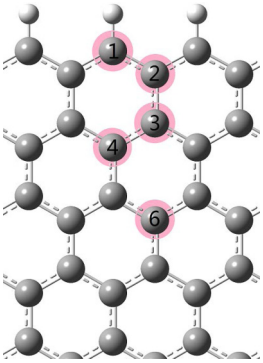

FIG. 9. (Color online) Schematic of the graphene zigzag edge.

For atomic and EC sites far from the edge, about 12 Å, the graphene ground-state potential is used. For sites near the edge, final-state-rule potentials have been generated using a 4×16 SC terminated by hydrogen on both sides (with 8 H and 64 C atoms) and one core hole on the absorbing site.

Figure 10 shows calculated unpolarized C K-edge XANES of individual C atoms at or near the graphene zigzag edge, in comparison with calculated XANES of infinite graphene and the experimental EELS spectrum of the individual outermost C atom at the edge taken from Ref. [44]. Our calculated spectra of edge carbon atoms are similar to calculated results in Refs. [44] and [45]. We found that XANES of the C atom labeled "6" is quite similar to XANES of infinite graphene, except that the whole spectrum is shifted a little toa lower energy. However, SC calculations with vacuum space cannot reproduce the absolute value of the potential with respect to the vacuum level precisely for low-dimensional systems, so that the accuracy of chemical shift between different structures is not ensured.

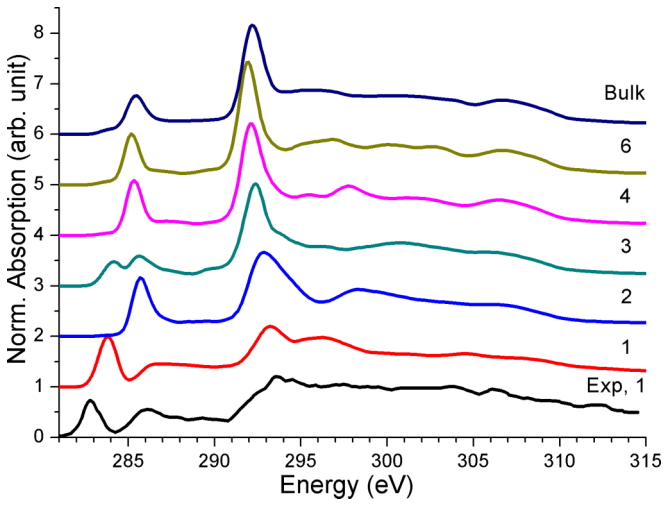

FIG. 10. (Color online) Calculated unpolarized C K-edge XANES of individual C atoms at or near the graphene zigzag edge, in comparison with the calculated XANES of infinite graphene ("bulk") and experimental EELS spectrum of the individual outermost C atom at the edge taken from Ref. [44]. Each number corresponds to the C atom which is labeled with the same number as in Fig. 9.

The overall spectral shape of the experimental spectrum, in particular, the edge-induced low-energy peak, is reproduced by the calculation. The main difference from the spectra of infinite graphene is the appearance of a new strong low-energy peak at 283.8 eV, which fits well the pre-edge peak (A2) position observed in some XANES experiments on graphene [see Table III and Fig. 4(a)] and has been attributed to a localized state at the Fermi level at the zigzag edge [46]. Experimentally, Refs. [43] and [47] have found that the more edge C atoms are probed in XAS, the higher is the intensity of the pre-edge peak. Moreover, other kinds of structure modulations like charged-species adsorption may also create such a pre-edge peak [43,48,49]. From all the experimental and theoretical evidence, it seems that the A2 peak is largely due to edge states or other structural modifications rather than being an intrinsic peak of perfect graphene.

There are some discrepancies of the peak positions between calculated and experimental spectra of the outermost edge C atom (labeled "1"), which is also true for another experiment [45]. The disagreement can be attributed to the following points: (i) Core-hole effects are not considered well as described in Sec. III. (ii) The potential generated by the VASP code may lead to some deviations, e.g., of the vacuum level, since the asymptotic behavior may be not reproduced well for low-dimensional systems in particular directions by the plane-wave method. (iii) The energy resolution of the experiment is 0.4 eV [44], which is not very fine. (iv) The absolute energy of the calculated spectrum is aligned according to experimental XANES of graphene from Ref. [25]. It is not surprising that there is ambiguity in the absolute energies of different experiments. For example, in Ref. [45], the energy position of peak π^* is fixed as 285.0 eV, which is different from the 285.5 eV [25] used in this work. (v) In reality, the edge structure is not as perfectly ordered as that of calculations; it can be distorted or not flat, so that the spectrum is modified. Moreover, the edge structure may be unstable under the incident electron beam [44]. (vi) The contribution of neighboring C atoms may be mixed in [45].

IV. OXYGEN ADSORPTION ON GRAPHENE

Among the various graphene derivatives, GO is the most important. Oxygen can be bound in different ways to C—on the basal plane, on the edge, or near vacancies—which makes this system quite complex. For simplicity, we focus on three types of basal-plane oxygen species: C-O-C (COC), C-OH (COH), and C=O (CO). This is suitable if the basal plane is complete so that there are few vacancies and the contribution of edge oxygen species can be negligible, which is the case for large samples.

We compare two structural models, STR1 and STR2, corresponding to low and high oxygen densities, respectively. In STR1, a single oxygen is put in the center of a large graphene cluster. In STR2, oxygen atoms are put in a periodic array on graphene, with 4 O atoms per $6\times6\times1$ SC, corresponding to an oxygen density of 5.3% (see Fig 12). The potential is constructed in the same fashion as before, e.g., for STR1, using final-state-rule potentials from a $4\times4\times1$ SC (see Fig. 11) VASP calculation for sites closer than 5 Å from the absorber and ground-state potential of the infinite graphene sheet for atoms

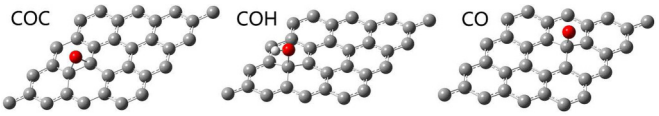

FIG. 11. (Color online) Supercells of three types of GO: gray, carbon; red, oxygen; white, hydrogen.

farther away. In both structural models, the cluster size of the XANES calculation is 20 Å, and the computational parameters are similar to those in the graphene case.

A. C K-edge XANES

In this section, we consider the low-density structure (STR1) and focus on the XANES spectrum of the C atom directly bonded to oxygen. First, we want to stress that SCF is important in this case, since in non-SCF-FP calculations (not shown), the main σ_z peaks of COC and COH are shifted to higher energies by about 1.5 eV compared with the SCF-FP results. In Fig. 13, σ_z values of COC and COH show a big peak near 288 and 288.5 eV, respectively, which fits the position of peak K. Combining the previous discussion in Sec. III, we make the following conclusions: (i) Since peak K does not arise for ideal graphene and is only weakly affected by stacking of graphene layers, the interpretation using the interlayer state [25,41] is probably not suitable. (ii) The finite size of and vacancies in the graphene sheet can lead to some oscillations between the two leading peaks, A and B, which may contribute to peak K. However, for the high-quality graphene sample, this kind of contribution is expected to be quite weak. (iii) Two typical oxygen species of GO adsorbed on the basal plane, C-O-C and C-OH, give rise to peak K, so that they are two possible origins of peak K in some experimental XANES of GO.

However, in cases where the proportion of oxygen is larger, other structural modulations can play important roles. In a considerable number of experiments [37,50–53], near 288 eV, we can observe a very pronounced and sharp peak at a higher energy and one or two broader peaks at lower energies. The broader peaks can be attributed to COC and COH bondings on the basal plane, while the sharp peak is normally attributed to the carboxylic acid group (-COOH) on the edge or near vacancies.

B. O K-edge XANES

In the MT approximation, the potential in the interstitial region is approximated by a constant. The choice of this parameter leads to an uncertainty in the energy scale and thus in chemical shifts. This ambiguity is absent in FPMS with space-filling cells, and as a result, chemical shifts become predictive and much more accurate than in the MT approximation. Further, since the structures of infinite graphene and GO studied in our work are similar, and we used vacuum spaces of the same size for the SC calculations, the chemical shift can be accurate.

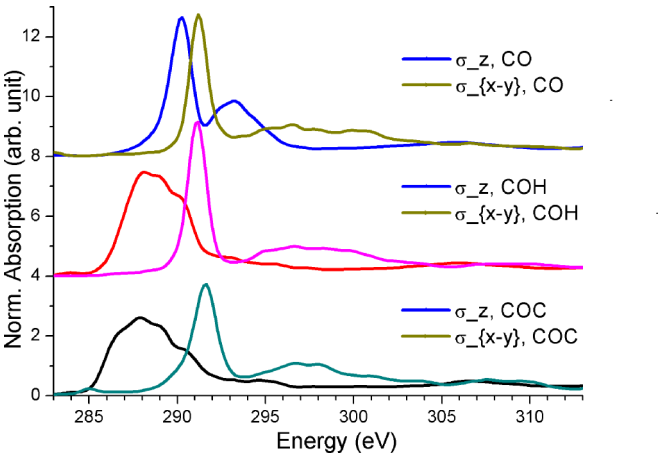

FIG. 13. (Color online) Calculation of polarization-dependent C K-edge XANES of carbon atoms directly bonded to oxygen, for three types of graphene oxide.

Figure 14 shows polarized XANES of COC, COH, and CO for the two structural models calculated in SCF-FP and for STR1 also in non-SCF-FP. The peak positions change quite strongly between SCF-FP and non-SCF-FP, which means that the use of the SCF potential is important in this case. There are also clear differences between the two structural models, indicating substantial interaction between adsorbed oxygen species in the high-density case (STR2), which leads to extra spectral fine structure.

Next, we have tried to simulate the experimental O K-edge XANES of GO at 800 °C in Ref. [50] shown in Fig. 15(c). This experiment was performed at a 90° incidence of the linearly polarized x rays so that σ_z should not contribute to the observed XANES. However, it can be seen in the left panel in Fig. 7 in this same Ref. [50] that the $1s\ \pi^*$ peak is fairly intense, which implies a non-negligible σ_z contribution. By fitting to the experimental spectrum, we find the weight of σ_z to be about 12%.

Cross sections of three oxygen species of two structural models are shown in Figs. 15(a) and 15(b). We have fitted the proportions of COC, COH, and CO to the experiment and obtained 44%, 56%, and 0% for STR1 and 33%, 67%, and 0% for STR2. The final XANES of both structural models is shown in Fig. 15(c). Since the concentration of oxygen is very low, there is an ambiguity in the intensity of the experimental spectra. Therefore, we have done the fittings to its derivative. Both calculations are qualitatively in accordance with the experiment. Moreover, the differences between the two calculated results are small. This implies that an oxygen concentration change of several percent will not affect the spectrum much.

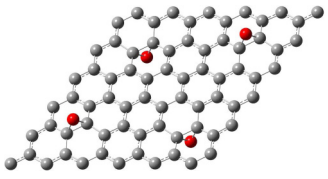

FIG. 12. (Color online) The supercell used for the calculation of COC-type graphene oxide in the high-density model (STR2), with C atoms shown in gray and O atoms in red.

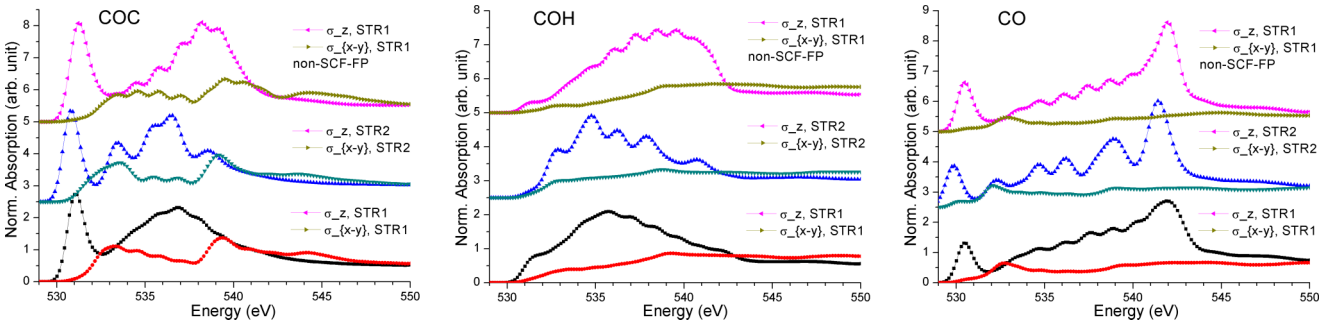

FIG. 14. (Color online) Calculated O K-edge XANES of GO with different structural models in SCF-FP and non-SCF-FP. STR1, the structure model containing only one oxygen atom; STR2, the structure model containing about 5.3% oxygen. Details about structural models are reported in Sec. IV.

V. COMPARISONS WITH OTHER METHODS

Here we compare the present FPMS results with three other theoretical methods.

A. Multiple scattering in the muffin-tin approximation

Following common practice, we have used slightly overlapping spheres in the MT calculation. Here the diameter of the spheres is taken to be 15% larger than the nearest-neighbor distance; i.e., the overlap factor (ovlp) is 1.15. Note that in FPMS, overlap between atomic cells is strictly 0, and when an overlap factor is indicated, it refers to the spheres in which the atomic cells are enclosed.

The spectra in Fig. 16 are plotted on the photoelectron final energy scale, without alignment to experiment, in order to see the peak shifts between different approximations. The SCF-FP calculation with space filling (bottom curve) gives by far the best results (see also Fig. 4). All other schemes, including SCF-FP without ECs, lack most of the fine structure in the energy range 5–20 eV. Therefore, both FP treatment inside each atomic cell and filling of interstitial space with ECs are necessary for accurate XANES. Compared with SCF-FP, all other spectra are shifted, especially those without ECs. This implies that for MS calculations without space filling, large errors in the absolute energy levels must be expected. Moreover, we have noted that the results obtained in the MT approximation are very sensitive to the constant interstitial potential and charge, which are usually treated as free parameters.

B. Density functional theory

In Refs. [5] and [56], the augmented plane-wave method and pseudopotential plane-wave method were used to calculate EELS of graphene, respectively. Their results are similar to ours. In Ref. [57], the authors have done DFT calculations in the low-energy region with the linear combination of atomic orbitals (LCAO) method to obtain initial- and final-state wave functions to compute the XAS of graphene. There are some differences between their and our results, e.g., related to layer effects. A drawback of the LCAO method is that uniform convergence of the types and amount of basis functions is not ensured [58,59] over the XANES energy range. This may lead to difficulties in studying XAS in graphene-related systems.

C. Projected-augmented-wave Green's function (PAW-GF) method

In Ref. [54], a scheme for XANES has been devised based on the recursion method. An advantage of this method is that the Hamiltonian needs to be diagonalized only for occupied states, while the core-level spectrum is computed as a continued fraction. In Fig. 17, C K-edge XANES of diamond calculated with the PAW-GF [54] and our SCF-FPMS methods are compared with experiment. The two theoretical spectra are very close. This may be expected since the charge densities are

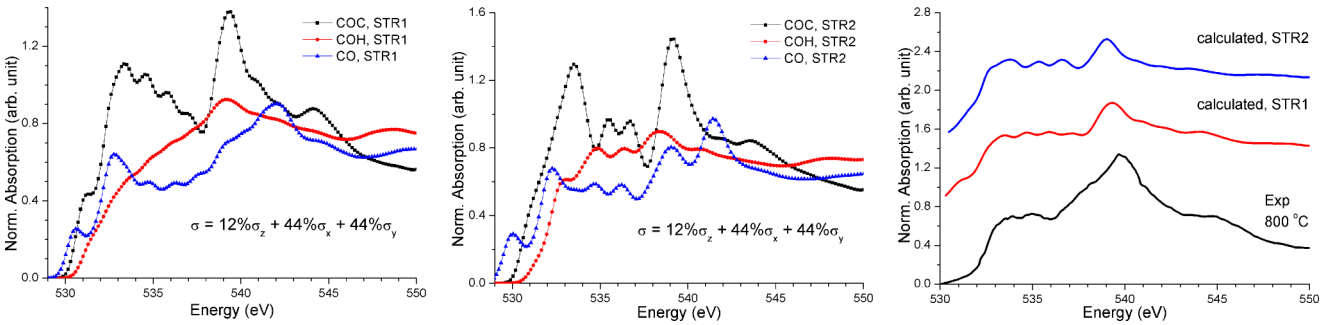

FIG. 15. (Color online) Calculated O K-edge polarized XANES of GO where the direction of the electric field is the same as in the experiment in [50] and the experiment shown in (b). (a) Using structural mode STR1, containing only one oxygen atom. (b) Using STR2, containing about 5.3% oxygen. (c) Weighted average of XANES of three types of GO using STR1 and STR2. The proportions of COC, COH, and CO obtained by fitting them to the experiment are 44%, 56%, and 0% for STR1 and 33%, 67%, and 0% for STR2.

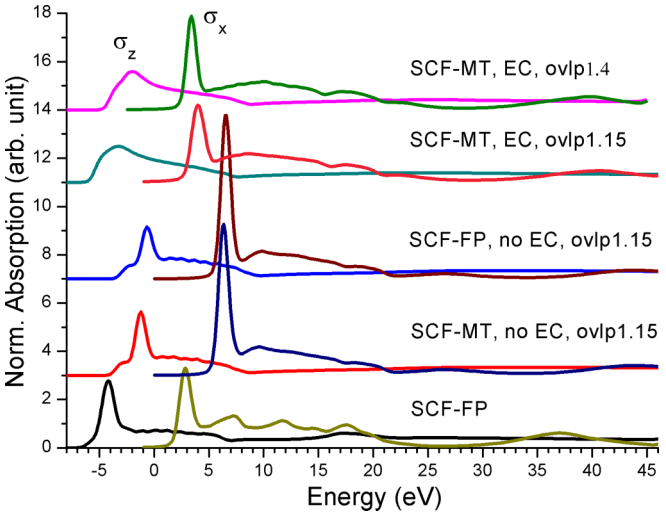

FIG. 16. (Color online) Calculated XANES of graphene in the SCF-FP and SCF-MT cases. The cluster size is always 25 Å. ovlp, overlap factor of spherical radii; EC, ECs added; no EC, ECs not added.

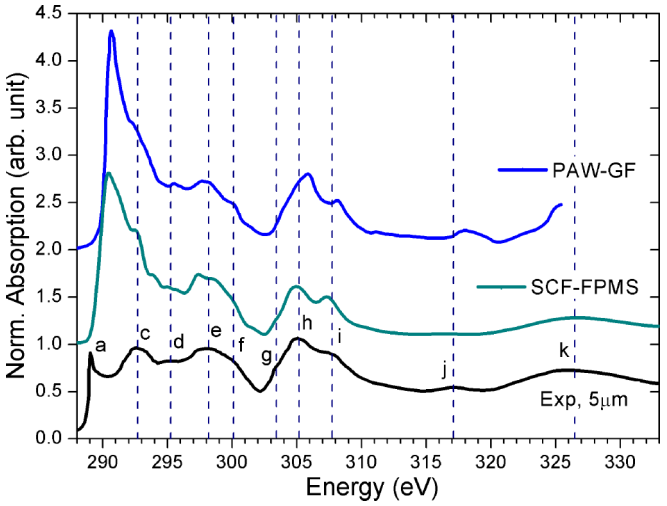

FIG. 17. (Color online) Calculated C K-edge XANES of diamond by PAW-GF [54] and our SCF-FPMS methods compared with the experiment from Ref. [55].

computed in the same way (PAW with a core hole in the SC). The almost-excellent agreement of the two spectra then clearly shows that in SCF-FPMS, potential generation and the change of boundary conditions from a *k*- to a real-space cluster method do not reduce the accuracy of the underlying PAW electronic structure calculation. This is an important check of our new method. While XANES calculations are numerically lighter in PAW-GF, a main advantage of SCF-FPMS is that it can directly be used for a variety of other electron spectroscopies (EXAXS, UPS, XPS, etc.), while this remains to be shown for PAW-GF. Further, when looking at the spectra in Fig. 17 in more detail, the SCF-FP spectrum compares slightly better with the experimental one beyond 302 eV. This might be due to the fact that in the PAW method the partial waves and projectors are fixed and adapted to the energy interval of the occupied valence electrons. This is not an issue in SCF-FPMS, since the all-electron potential is used for solving the Schrödinger equation of the continuum states.

VI. CONCLUSION

We have presented FPMS calculations for XANES of graphene and related systems. The potentials were generated from self-consistent charge densities obtained through plane-wave PAW calculations with the VASP code. With this new scheme C and O K-edge XANES has been studied for graphene, FLG, graphite, three types of GO, and the zigzag edge of graphene, and results have been compared with experiments and several other theoretical methods. With the present FP method, good agreement with experiment has been obtained for all systems, while conventional MT calculations give poor results. The main variation of the XANES spectra as a function of the number of graphene layers has been successfully reproduced. The analysis of C K-edge XANES in graphene edge atoms and that of GO have helped to clarify the origin of several controversial peaks in the graphene spectrum, especially the pre-edge shoulder (A2) and the so-called interlayer-state peak (K). By calculating the O K-edge XANES of three types of GO, we have shown that the proportion of different oxygen species can be estimated by a fit to the experimental spectrum.

ACKNOWLEDGMENTS

We would like to thank T. Konishi and W. Huang for illuminating discussions. Computational resources of the USTC supercomputing center are gratefully acknowledged. Parts of this work were funded by the European FP7 MSNano network under Grant Agreement No. PIRSES-GA-2012-317554, by COST Action MP1306 EUSpec, and by JSPS KAKENHI Grant No. 25887008. K. Hatada gratefully acknowledges the support from Marie Curie Intra-European Fellowship MS-BEEM (No. PIEF-GA-2013-625388).

[1] A. Neto, F. Guinea, N. Peres, K. S. Novoselov, and A. K. Geim, Rev. Mod. Phys. **81**, 109 (2009).
[2] L. S. Zhang, X. Q. Liang, W. G. Song, and Z. Y. Wu, Phys. Chem. Chem. Phys. **12**, 12055 (2010).
[3] D. Haberer, D. V. Vyalikh, S. Taioli, B. Dora, M. Farjam, J. Fink, D. Marchenko, T. Pichler, K. Ziegler, S. Simonucci, M. S. Dresselhaus, M. Knupfer, B. Buchner, and A. Gruneis, Nano Lett. **10**, 3360 (2010).
[4] S. Bhowmick, J. Rusz, and O. Eriksson, Phys. Rev. B **87**, 155108 (2013).
[5] G. Bertoni, L. Calmels, A. Altibelli, and V. Serin, Phys. Rev. B **71**, 075402 (2005).
[6] Q. Li, Y. Ma, A. R. Oganov, H. Wang, H. Wang, Y. Xu, T. Cui, H.-K. Mao, and G. Zou, Phys. Rev. Lett. **102**, 175506 (2009).
[7] K. Hatada, K. Hayakawa, M. Benfatto, and C. R. Natoli, J. Phys.: Condens. Matter **22**, 185501 (2010).

[8] K. Hatada, K. Hayakawa, M. Benfatto, and C. R. Natoli, Phys. Rev. B **76**, 060102 (2007).
[9] P. E. Blöchl, Phys. Rev. B **50**, 17953 (1994).
[10] A. R. Williams *et al.*, J. Phys. C: Solid State Phys. **7**, 37 (1974).
[11] A. Gonis and W. H. Butler, *Multiple Scattering in Solids* (Springer, Berlin, 2000).
[12] C. R. Natoli, M. Benfatto, C. Brouder, M. F. R. López, and D. L. Foulis, Phys. Rev. B **42**, 1944 (1990).
[13] D. L. Foulis, arXiv:0806.0574.
[14] A. L. Ankudinov and J. J. Rehr, Phys. Scr. **T115**, 24 (2005).
[15] T. Huhne and H. Ebert, Solid State Commun. **109**, 577 (1999).
[16] G. Kresse and D. Joubert, Phys. Rev. B **59**, 1758 (1999).
[17] V. I. Lebedev, USSR Comput. Math. Math. Phys. **15**, 44 (1975).
[18] L. Hedin, Phys. Rev. **139**, A796 (1965).
[19] T. X. Carroll, J. Hahne, T. D. Thomas, L. J. Saethre, N. Berrah, J. Bozek, and E. Kukk, Phys. Rev. A **61**, 042503 (2000).
[20] M. Coville and T. D. Thomas, Phys. Rev. A **43**, 6053 (1991).
[21] M. Coreno, M. De Simone, K. C. Prince, R. Richter, M. Vondráček, L. Avaldi, and R. Camilloni, Chem. Phys. Lett. **306**, 269 (1999).
[22] A. Goldoni, R. Larciprete, L. Gregoratti, B. Kaulich, M. Kiskinova, Y. Zhang, H. Dai, L. Sangaletti, and F. Parmigiani, Appl. Phys. Lett. **80**, 2165 (2002).
[23] F. Sette, G. K. Wertheim, Y. Ma, G. Meigs, S. Modesti, and C. T. Chen, Phys. Rev. B **41**, 9766 (1990).
[24] J. P. Perdew, J. A. Chevary, S. H. Vosko, K. A. Jackson, M. R. Pederson, D. J. Singh, and C. Fiolhais, Phys. Rev. B **46**, 6671 (1992).
[25] D. Pacilé, M. Papagno, A. Fraile Rodríguez, M. Grioni, L. Papagno, Ç. Ö. Girit, J. C. Meyer, G. E. Begtrup, and A. Zettl, Phys. Rev. Lett. **101**, 066806 (2008).
[26] M. Papagno, A. Fraile Rodríguez, Ç. Ö. Girit, J. C. Meyer, A. Zettl, and D. Pacilé, Chem. Phys. Lett. **475**, 269 (2009).
[27] Y. Ma, P. Skytt, N. Wassdahl, P. Glans, J. Guo, and J. Nordgren, Phys. Rev. Lett. **71**, 3725 (1993).
[28] F. Mauri and R. Car, Phys. Rev. Lett. **75**, 3166 (1995).
[29] M. Ishigami, J. H. Chen, W. G. Cullen, M. S. Fuhrer, and E. D. Williams, Nano Lett. **7**, 1643 (2007).
[30] P. Krüger and C. R. Natoli, Phys. Rev. B **70**, 245120 (2004).
[31] G. Onida, L. Reining, and A. Rubio, Rev. Mod. Phys. **74**, 601 (2002).
[32] J. Vinson, J. J. Rehr, J. J. Kas, and E. L. Shirley, Phys. Rev. B **83**, 115106 (2011).
[33] W. Olovsson, I. Tanaka, T. Mizoguchi, P. Puschnig, and C. Ambrosch-Draxl, Phys. Rev. B **79**, 041102 (2009).
[34] E. L. Shirley, Phys. Rev. Lett. **80**, 794 (1998).
[35] S. B. Trickey, F. Müller-Plathe, G. H. F. Diercksen, and J. C. Boettger, Phys. Rev. B **45**, 4460 (1992).
[36] E. Duplock, M. Scheffler, and P. Lindan, Phys. Rev. Lett. **92**, 225502 (2004).
[37] V. A. Coleman, R. Knut, O. Karis, H. Grennberg, U. Jansson, R. Quinlan, B. C. Holloway, B. Sanyal, and O. Eriksson, J. Phys. D: Appl. Phys. **41**, 062001 (2008).
[38] M. Klintenberg, S. Lebegue, C. Ortiz, B. Sanyal, J. Fransson, and O. Eriksson, J. Phys.: Condens. Matter **21**, 335502 (2009).
[39] M. Abbas, Z. Y. Wu, J. Zhong, K. Ibrahim, A. Fiori, S. Orlanducci, V. Sessa, M. L. Terranova, and I. Davoli, Appl. Phys. Lett. **87**, 051923 (2005).
[40] H.-K. Jeong, H.-J. Noh, J.-Y. Kim, L. Colakerol, P.-A. Glans, M. H. Jin, K. E. Smith, and Y. H. Lee, Phys. Rev. Lett. **102**, 099701 (2009).
[41] V. N. Strocov, P. Blaha, H. I. Starnberg, M. Rohlfing, R. Claessen, J. M. Debever, and J. M. Themlin, Phys. Rev. B **61**, 4994 (2000).
[42] R. Rosenberg, P. Love, and V. Rehn, Phys. Rev. B **33**, 4034 (1986).
[43] B. J. Schultz, C. J. Patridge, V. Lee, C. Jaye, P. S. Lysaght, C. Smith, J. Barnett, D. A. Fischer, D. Prendergast, and S. Banerjee, Nat. Commun. **2**, 372 (2011).
[44] K. Suenaga and M. Koshino, Nature **468**, 1088 (2010).
[45] J. H. Warner, Y. C. Lin, K. He, M. Koshino, and K. Suenaga, Nano Lett. **14**, 6155 (2014).
[46] K. Nakada, M. Fujita, G. Dresselhaus, and M. S. Dresselhaus, Phys. Rev. B **54**, 17954 (1996).
[47] S. Entani, S. Ikeda, M. Kiguchi, K. Saiki, G. Yoshikawa, I. Nakai, H. Kondoh, and T. Ohta, Appl. Phys. Lett. **88**, 153126 (2006).
[48] X. Liu, T. Pichler, M. Knupfer, J. Fink, and H. Kataura, Phys. Rev. B **70**, 205405 (2004).
[49] A. Preobrajenski, M. Ng, A. Vinogradov, and N. Mårtensson, Phys. Rev. B **78**, 073401 (2008).
[50] A. Ganguly, S. Sharma, P. Papakonstantinou, and J. Hamilton, J. Phys. Chem. C **115**, 17009 (2011).
[51] H. K. Jeong, H. J. Noh, J. Y. Kim, M. H. Jin, C. Y. Park, and Y. H. Lee, Europhys. Lett. **82**, 67004 (2008).
[52] V. Lee, L. Whittaker, C. Jaye, K. M. Baroudi, D. A. Fischer, and S. Banerjee, Chem. Mater. **21**, 3905 (2009).
[53] S. Banerjee, T. Hemraj-Benny, M. Balasubramanian, D. A. Fischer, J. A. Misewich, and S. S. Wong, Chem. Commun. (Cambr.) **7**, 772 (2004).
[54] M. Taillefumier, D. Cabaret, A. M. Flank, and F. Mauri, Phys. Rev. B **66**, 195107 (2002).
[55] Y. K. Chang, H. H. Hsieh, W. F. Pong, M. H. Tsai, F. Z. Chien, P. K. Tseng, L. C. Chen, T. Y. Wang, K. H. Chen, D. M. Bhusari *et al.*, Phys. Rev. Lett. **82**, 5377 (1999).
[56] J. Lu, S. P. Gao, and J. Yuan, Ultramicroscopy **112**, 61 (2012).
[57] W. Hua, B. Gao, S. Li, H. Ågren, and Y. Luo, Phys. Rev. B **82**, 155433 (2010).
[58] M. Iannuzzi and J. Hutter, Phys. Chem. Chem. Phys. **9**, 1599 (2007).
[59] B. Brena, S. Carniato, and Y. Luo, J. Chem. Phys. **122**, 184316 (2005).